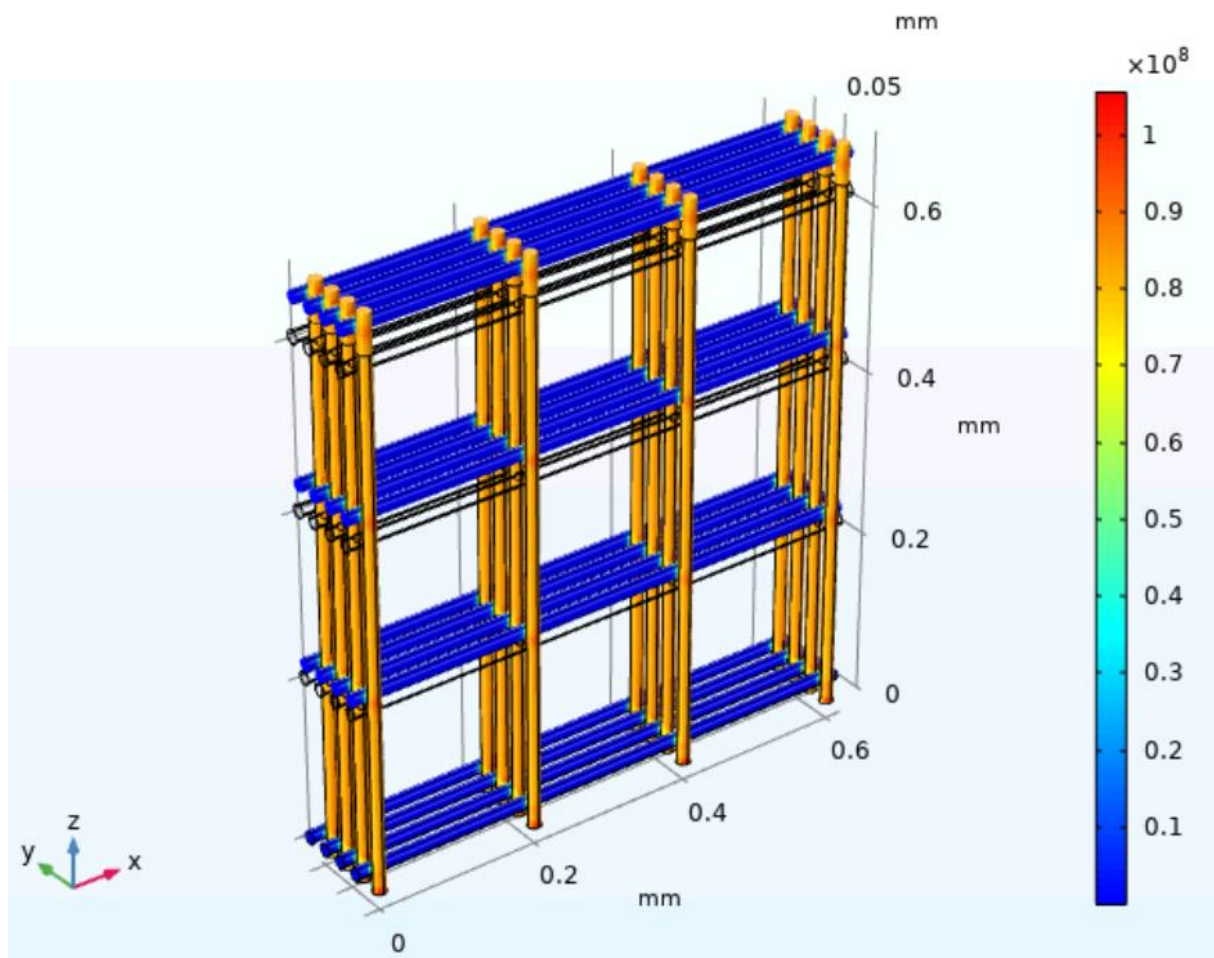


Computational modelling of scaffolds for interfacial tissue engineering



Name: Timo Rikmanspoel

Student number: S3501930

Research group: Zernike Institute for Advanced Materials

Examiner: Prof. dr. Marco Harmsen

Supervisors: Dr. Malgorzata Wlodarczyk-Biegun,

Piotr Zielinski

Acknowledgements

Throughout the writing of this research paper I have received a great amount of support and assistance.

I would first like to thank my supervisors Piotr Zielinski and Dr. Malgorzata Wlodarczyk-Biegun. You were always open for questions. Your great feedback and expertise were really helpful in both performing my research and writing the report. It was very nice working together with you.

I would also like to thank my study mentor Prof. dr. Marco Harmsen. You were always very responsive and open to questions and offered great help in structuring my research. Furthermore, the discussions about the biological aspects of my research were always really interesting and sharpened my thinking about the project.

In addition I would like to thank Marcus Koch (INM-Leibniz Institute for New Materials in Germany) for his great help in making SEM pictures of my scaffolds. It was great to have the opportunity to obtain SEM pictures of my scaffolds.

Abstract

In the human body, hard soft-tissue interfaces are the connections between hard and soft tissues such as tendon and bone. They are composed of different mechanical and biochemical properties, and while the connection is strong, it still remains prone to injuries. The bone-tendon hard-soft tissue interface consists of 4 zones with different mechanical properties. The gradual change in properties helps with better transferring the load during movement.

In my study I aim at developing scaffolds that mimic the native gradient structure in hard-soft tissue interface. For scaffold production, Melt Electrowriting (MEW) is used to produce fibrous scaffolds from polycaprolactone (PCL). Scaffolds with different designs were printed, including designs with gradually changing architecture. To examine if the scaffolds are suitable for hard-soft tissue applications, mechanical tests on the scaffolds were performed (e.g. tensile test). However, these tests are mostly destructive methods. Therefore, in this research, to support experimental data, computer simulations in COMSOL were established. With the use of these simulations, mechanical properties of the scaffolds can be predicted. These computer simulations can be a powerful tool to save both time and materials. Finally, cell culture was performed to examine if the proposed scaffolds are relevant for application in regenerative medicine.

Table of contents

1 Introduction.....	6
2 Materials and methods	9
2.1 MEW	9
2.1.1 Fabrication of scaffolds	9
2.1.2 Morphology of the scaffolds	9
2.2 SEM.....	9
2.3 Mechanical testing	10
2.4 Computational modelling.....	10
2.4.1 Finite element modelling (FEM)	10
2.4.2 Geometry.....	11
2.4.3 Material properties	11
2.4.4 Calculations	12
2.5 Application.....	12
2.6 Cell studies.....	12
2.6.1 Cell culture.....	12
2.6.2 Cell viability: Live/dead staining	12
2.6.3 Cell adhesion	13
2.6.4 Cell proliferation.....	13
2.7 Statistical analysis.....	13
3 Results	14
3.1 MEW	14
3.2 Cell studies.....	17
3.3 FEM.....	18
3.4 Application.....	18
4 Discussion and conclusion	20
6 References	23
Appendix A Report COMSOL model	25
1 Global Definitions	27
1.1 Parameters	27
2 Component 1.....	28
2.1 Definitions	28
2.1.1 Coordinate Systems.....	28
2.2 Geometry 1.....	28
2.3 Materials.....	29
2.3.1 PCL.....	29

2.4	Solid Mechanics.....	29
2.4.1	Linear Elastic Material 1	30
2.4.2	Fixed Constraint 1.....	30
2.4.3	Prescribed Displacement 1.....	30
2.5	Mesh 1.....	30
3	Study 1.....	31
3.1	Stationary	31
3.1.1	Study extensions.....	31
4	Results	33
4.1	Datasets.....	33
4.1.1	Study 1/Solution 1	33
4.2	Derived Values.....	33
4.2.1	Surface Integration 1	33
4.2.2	Surface Average 1.....	34
4.3	Tables.....	34
4.3.1	Table 1	34
4.4	Plot Groups.....	35
4.4.1	Stress (solid)	35

1 Introduction

An increase in tendon injuries has been observed for decades [2, 3]. Tendon injuries are responsible for an estimated 30-50% of all sports related injuries [3]. In the human body, the tendon is attached firmly to the bone. While this connection is strong, the hard-soft tissue interface still remains prone to injuries. An example of hard-soft tissue injuries is tendon rupture, which can happen in the Achilles. This can be caused by an unexpected, forced movement of the feet [4]. These unexpected movements of the feet often occur during sports where sudden jumping or sprinting is needed. According to European study badminton, handball and football are high risk sports concerning Achilles tendon ruptures, while American studies indicate basketball as the sport which leads to the most of these injuries [5, 6]. Moreover, the rupture occurs mostly in people aged 30-49 years old and rather in men than in women [5]. Besides the Achilles tendon, there are also many other places in the human body where severe tendon ruptures can occur. Currently, sutures are used to heal these injuries. However, the disadvantage of sutures is that they lead to high stress concentration which might cause surgery failure [7]. Therefore, current strategies are still not optimal. Thus, it is necessary to search for new methods to treat these injuries. This is where tissue engineering can play a big role. Different aspects of tissue engineering are engineering cells, materials and tissue architecture [8]. Tissues can be enhanced, maintained or restored by tissue engineering [9]. One of the principles of tissue engineering is creating biological substitutes. These substitutes can be valuable treatments for hard-soft tissue interface injuries.

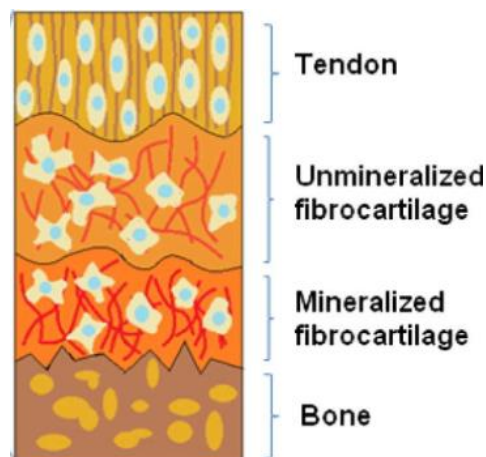


Figure 1. Schematic representation of the 4 different zones of hard soft tissue interface. Going from tendon towards mineralized fibrocartilage, the fibers (red and purple lines) are getting less aligned. The yellow dots with a blue centre represents the cells. Reprinted from 'Gradient biomaterials for soft-to-hard interface tissue engineering' by Seidi et al., 2010, Acta Biomaterialia. [1].

To understand how tissue engineering is able to help, first a closer look into the hard-soft tissue interfaces is needed. The bone-tendon connection consists of 4 zones. Going from hard to soft tissue the following 4 zones will be encountered consequently: bone, mineralized fibrocartilage, nonmineralized fibrocartilage and tendon (Fig. 1). Across these zones the elastic modulus changes gradually. This gradual change helps the tissue with better transferring loads. It can withstand more shear stress and compression. Tendons have an important purpose in transferring force from muscles to bones while using this force to move the skeleton. These high forces from the tendons need to be transferred to the bone without damaging the bone. That is why the hard-soft tissue interface changes gradually. In the human body tendons fulfil this force transferring purpose by having a high uniaxial strength, which is supplied by many collagen type I molecules laying aligned next to each other. These collagen type I fibers are arranged in the direction of the force [10, 11]. The tendon interface of the

hard-soft tissue is fibrous and stretchable. In the uncalcified fibrocartilage the collagen fiber bundles are less parallel than the bundles in the tendon. Collagen type I and II can be found in this zone. The cells in the uncalcified fibrocartilage are organized in longitudinal rows. They are surrounded by moderate levels of extracellular matrix (ECM). A tidemark indicates where the calcification starts and thus the uncalcified zone ends. The collagen fibers pass this tidemark uninterrupted mainly in an angle of approximately 90 degree [12]. In the calcified fibrocartilage zone there are collagen fibers of types I, II and X. In this zone there is also mineralized tissue [13]. On the opposite site of the tendon, there is the bone site, which is calcified and stiff. In the bone tissue osteoblast, osteoclast and osteocytes can be found, together with mineralized collagen I fibers. There are no Collagen type II fibers in the bone zone [14]. This shows that in hard-soft tissue interface gradients in mechanical properties can be observed. The average Young's modulus in a (Achilles) tendon is $220,2 \pm 83,3$ MPa [15]. The average Young's modulus in the fibrocartilage varies between 76 and 122 MPa. In the bone site the average Young's modulus varies between 939 and 1393 MPa. Therefore, the scaffold representing a hard-soft tissue interface should probably have a total Young's modulus gradient in the range of 76 and 1393 MPa [16].

Problems with a gradual structure like described above is that they are very difficult to treat. Healing of the hard-soft tissue interfaces after injuries can lead to scar tissue formation instead of regrowth of the original tissue. Therefore, there is a high chance of recurrence of the rupture because the tissue of the interface is not fully regenerated [17]. Furthermore, due to a low metabolic rate, tendons have bad healing properties. This causes a slow healing after injury [18]. An ideal treatment should consist of a structure which mimics both the biological and mechanical properties of the native interface. This structure should be able to be implanted. It can connect the hard part of the tissue with the soft part. Because of the gradient in this structure, it will make a good connection between the tissues.

For this use Melt Electrowriting (MEW) has great potential because it allows the production of gradient structures. MEW is a technique which makes it possible to create scaffolds with highly complex structures. MEW is a 3D printing method which is used to deposit fibers with highly precise accuracy. Up to 50 layers can be printed with minimal defects [19]. The cartridge is loaded with a polymer and a temperature higher than the melting point of the polymer is applied. The molten polymer is pushed through the nozzle due to air pressure and pulled towards the collector due to an electrical field between the nozzle and a grounded collector plate. Variables like air pressure, voltage, temperature and distance of the printing nozzle to the collector can be changed. A MEW device is able to deposit fibers on a collector plate following a prescribed pathway. This makes it possible to print different designs and structures.

Printing scaffolds can take a few minutes to several hours, depending mainly on the size of the scaffold. One of the factors which influences how much time it takes to print a scaffold is the printing speed. Printing at high speeds can save time. However, the deposition of the fibers can be less accurate. Hence, it is important to find a good printing speed at which the fibers will still be deposited in an accurate manner. While searching for scaffolds which can closely mimic the hard-soft tissue interface, mechanical tensile testing is useful to examine the mechanical properties of a scaffold. However, mechanical testing is a destructive method. Due to this, it can be really useful if mechanical properties of scaffolds can be predicted before printing.

This is where computer simulation can play a big role. Within computational modelling software, a model of a given material can be created and various physics phenomena can be applied to the model. A model which is able to simulate what will happen to scaffolds when they are stretched and also obtain a Young's modulus from this scaffold would be very beneficial. In addition to this, it would be useful if important properties of the scaffold model could be changed easily. Examples of these properties are fiber thickness, number of layers and material properties. By making use of computer simulation, mechanical properties of samples can be predicted quickly before printing and mechanical testing. Therefore, computer simulation can be a powerful tool for tissue engineering and 3D printing if the experimental data matches with data from the model.

Hard-soft tissue consists of multiple zones with varying properties. The model can assist in the process of making designs for these interfaces, by predicting mechanical properties of the designs. In general, a model can also be a great help in creating fibrous scaffolds for interfaces where mechanical tensile properties play an essential role. With the use of modelling the design can be adjusted to reach properties similar to native tissue.

The aim of this research was to show how computational modelling can support 3D printing of scaffolds and show how the mechanical properties of the chosen design match those in the interfacial tissues. Biological tests were performed to show the application potential of the printed scaffolds in tissue engineering.

2 Materials and methods

2.1 MEW

2.1.1 Fabrication of scaffolds

All scaffolds created in this project were made of polycaprolactone (PCL, PURASORB[®] PC 12, Corbion). All scaffolds were fabricated using a MEW device (Spraybase[®] A-1204-0001-01D). First, 2 layered scaffolds (500 μm interfiber distance) were printed with a varying collector speed ranging from 20 to 120 mm/s, to examine the effect of the collector speed on the printing accuracy. Furthermore, scaffolds with different pore sizes (100, 200 and 300 μm) and amount of layers (8, 16 and 24 layers) were fabricated to investigate the fiber alignment in these scaffolds. In addition to this, the possibilities of MEW to create other structures rather than squares were investigated by printing 8 layered rhombus structures (70° angle, 500 μm interfiber distance). For the final scaffolds the following printing parameters have been used:

- Working distance: 4 mm
- Nozzle temperature: 100 degree Celsius
- Temperature in the cartridge: 100 degree Celsius
- Voltage: 6 kV
- Pressure: 0,15 bar, adjusted to 0,210-0,215 bar during the experiment to maintain the same fiber thickness
- Collector speed: 25 mm/s
- Nozzle type: 0,3 mm diameter, bras nozzle (E3D-ONLINE)

When printing, a sacrificial zone of straight lines has been used to stabilize the jet before printing the scaffold. For the final design 2 gradient scaffolds were printed. Both consisted of three different zones. In each zone there was a difference in the interfiber distance in the rhombus and or the square/rectangular mesh. The scaffolds with the varying interfiber distance in each zone are described below. In the gradient scaffolds each zone represents a zone in the native hard soft tissue interface. Zone 1 (highest interfiber distance) represents the tendon site, zone 2 (average interfiber distance) represents the (un)calcified fibrocartilage site and zone 3 (lowest interfiber distance) represents the bone site.

Gradient 1:

- Zone 1: square 250 μm , rhombus 1250 μm (Fig. 5A)
- Zone 2: square 250 μm , rhombus 500 μm (Fig. 5B)
- Zone 3: square 250 μm , rhombus 250 μm (Fig. 5C)

Gradient 2:

- Zone 1: rectangular 250x1000 μm , rhombus 500 μm (Fig. 5H)
- Zone 2: rectangular 250x500 μm , rhombus 500 μm (Fig. 5I)
- Zone 3: square 250x250 μm , rhombus 250 μm (Fig. 5J)

All of the rhombus structures have a 159° angle.

2.1.2 Morphology of the scaffolds

The scaffolds were examined with a light microscope (Nikon SMZ-2T). The microscope was used to visualize the fibers alignment. The inter-fiber distance and fiber diameters were measured using MOTIC software.

2.2 SEM

Scanning electron microscopy (SEM) pictures were used to determine how the fibers are interconnected and to visualize what happens at the nodes when after tensile testing was performed. Prior to imaging, samples were gold coated using gold sputtering (20mA, 35s). The samples were

visualized using SEM (FEI Quanta 400 FEG) under high vacuum conditions (SE detection, 3 kV accelerating voltage).

2.3 Mechanical testing

Uniaxial tensile tests were performed to investigate the mechanical properties of the scaffolds. An Instron 5565 tensile testing device with a 100N loading cell was used. The scaffolds were fixed in the pneumatic clamps (0,4 bar) and stretched with a strain rate of 20 mm/s. The experiment was performed until failure. For these tests, scaffolds were cut in rectangular shapes. The width, thickness and length of the sample were measured before testing. 3 samples of each scaffold design were tested. All tensile testing experiments were performed at room temperature. The Young's modulus was calculated from the linear part of the stress/strain curve. The equation (1) for the Young's modulus (E) is:

$$E = (F/A)/(\Delta L/L) \quad (1)$$

where F is the applied force, ΔL is the change in length, L is the initial length, A is the cross-sectional area of the sample.

2.4 Computational modelling

2.4.1 Finite element modelling (FEM)

Table 1. All parameters used in the model.

Name	Expression	Value	Description
width	h1	6.4E-4 m	Dimension of the model (x-direction)
thickness	y_num*y_dis + 2*con	1.16E-4 m	Dimension of the model (y-direction)
surface_area	width*thickness	7.424E-8 m ²	Cross section area of the model
con	2[μ m]	2E-6 m	Amount of connection between fibers
dens1	1145	1145	Density
disp	0.3[mm]	3E-4 m	Displacement
y_dis	(2*rad1) - con	1.4E-5 m	Distance between layers
x_dis	0.2[mm]	2E-4 m	Distance between the (centers of) fibers, pore size
h1	x_num*x_dis - ((4/5)*x_dis)	6.4E-4 m	Length of the fibers
x_num	4	4	Number of fibers next to each other
y_num	8	8	Number of layers of the scaffold
pois1	0.3	0.3	Poisson's ratio
rad1	0.008[mm]	8E-6 m	Radius of the fibers
E1	178.817[MPa]	1.7882E8 Pa	Young's modulus material

To predict the mechanical properties of the scaffolds, specifically Young's modulus value and stress accumulation points, computer simulations were used. For these simulations, a 3D model was created in the COMSOL Multiphysics® version 5.5. The module *Structural Mechanics* was used, which can be used to examine the deformations, strains and stresses of solid structures. Within the structural mechanics module, a stationary study was performed, in which the assumption is made that field variables do not change over time. The process of finding the right design can have an iterative nature. Therefore, most variables are declared as a parameter in the model. The parameters were declared in a way that a new scaffold model with varying topology could be created just by changing the parameters of the model. Thus, if a model needs to be created with e.g. a different amount of layers, just the corresponding parameter y_num , (Table. 1) needs to be changed. Hence, the model would update automatically. All parameters used in the model can be found in Table 1.

2.4.2 Geometry

In the model, the structure of the scaffold is represented as a geometry.

For this model, solid cylinders were used to represent the MEW fibers. A structure was built where each layer consists of three fibers placed in one direction. The fibers were placed consecutively in X- or Z-direction. This way a square mesh structure was created (Fig. 2). The final amount of layers can be set by changing the corresponding parameter (y_num). The overlapping of the fibers was set for $2\mu\text{m}$ to ensure the connection between the fibers. Models of scaffolds (8 layers, $16\mu\text{m}$ fiber diameter) with the following pore sizes were created: $200\mu\text{m}$, $300\mu\text{m}$, $500\mu\text{m}$ to compare with the mechanical tensile testing results.

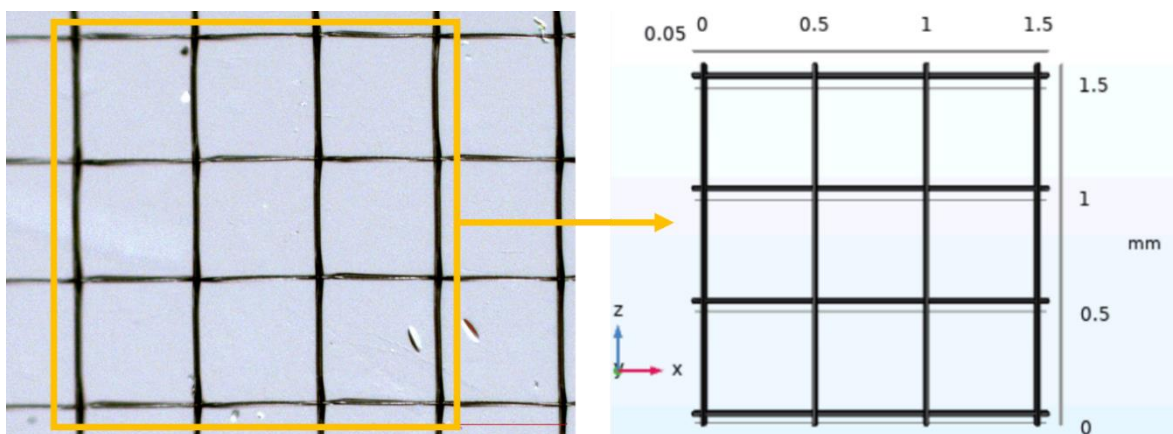


Figure 2. From scaffold to model. On the left, 8 layered scaffold with a $500\mu\text{m}$ pore size. On the right the corresponding geometry as used in the model for this scaffold.

2.4.3 Material properties

Once the geometry is created, material properties can be applied on this geometry, which allow the model to calculate the mechanical values. Therefore, it is necessary to define the material of the model- polycaprolactone (PCL). Since PCL is not in the standard material library of COMSOL it is necessary to create a PCL material and assign properties to it. To make the model as close as possible to the experimental data, material properties from the PCL used in this research were determined and implemented in the model. Thick fibers ($d=0,8\mu\text{m}$) of PCL were printed using MEW. The mechanical properties of these thick fibers were examined using tensile testing to obtain a Young's modulus. The Young's modulus was calculated from the linear slope of the stress-strain curve using equation (1) and implemented in the model. The PCL properties in the model are as follows: Young's modulus ($178,817\text{ [MPa]}$), density (1145 [kgm-3]), Poisson's ratio ($0,3\text{ [-]}$) [20, 21].

2.4.4 Calculations

In this study a fine mesh was used for the calculations. In the model, one end of the scaffold was fixed. On the opposite end a prescribed displacement was applied. The final displacement was set to 0,3 mm. Steps of 0,02 mm were used. A stress plot is created together with a table of the stress/strain values for each displacement step. Eventually, the goal of this study's computer model was to analyse the linear part of the stress-strain curve and obtain a scaffold's Young's modulus. This is the first part of a stress strain curve; the deformation is still elastic in this region. The values of this part of the region can be found in the table with the stress-strain values, and from this table the Young's modulus can be calculated.

2.5 Application

In this research an application was created which allows to change the following parameters:

- Number of layers in the scaffold
- Radius of the fibers
- Amount of connection between layers
- Young's modulus

The application allows users to create a geometry and calculate the force, stress and strain for a defined displacement. Moreover, a report can be created with all the results and more detailed information about the model behind the application.

2.6 Cell studies

2.6.1 Cell culture

Three different groups, each consisting of three scaffolds were used. 8 layered scaffolds were used with a 200 μm square pore size. Three groups of PCL scaffolds were used: untreated, plasma treated and gelatin coated. The first group consisted of untreated PCL scaffolds. The scaffolds in the second group were covered with gelatin. Gelatin (MERCK) was dissolved in distilled water in order to get a 10% w/v solution. This solution was autoclaved for 30 minutes in 121 °C. 220 μl of the 10% w/v gelatin solution was added to the wells with the scaffolds. The scaffolds were incubated for two hours with the gelatin solution. After incubation the scaffolds were transferred to a new 24 well plate (662260, Greiner Bio-One). The third group of scaffolds was sent to plasma treatment. The device used for plasma treatment was PDC-002, Harrick Plasma, USA. These scaffolds were placed in the plasma chamber and a vacuum was applied for 2 minutes before treatment. Then an air plasma was applied for 5 minutes using a high voltage.

All of the scaffolds were placed in a 24-well plate. A rubber o-ring was placed on top of each scaffold to prevent the scaffolds from floating. The scaffolds were sterilized in the wells in 1 ml 70% v/v ethanol for 25 minutes. After sterilisation, the scaffolds were washed three times with 1,5 ml Dulbecco's Phosphate-Buffered Saline (DPBS) (Sigma-Aldrich) to ensure there was no ethanol left in the wells. Fibroblasts derived from Swiss albino mice embryos (NIH-3T3 cells) (CRL-1658, ATCC) were seeded on top of the scaffolds. A seeding density of 150.000 cells per well was used. After seeding, the well plate with scaffolds with cells was placed in an incubator (37 degrees, 95% air / 5% Co₂) for 2 hours to ensure the cells had time to attach to the scaffold. After that time, 1ml of cell culture medium containing DMEM (Gibco) (10 vol.% FCS, 1vol.% Glutamax (gibco), 1 vol.% Penstrep (Gibco) and 1 ng/ml fibroblast growth factor(Gibco)) was added to each well. The medium was changed after day 1, 3, 4 and 7. Between experiments all cells were stored in an incubator (37 degrees, 95% air / 5% Co₂).

2.6.2 Cell viability: Live/dead staining

A live/dead assay was done as described in the protocol established by K.H. Jones and J.A Senft [22]. In addition to the three scaffold groups, three control groups were used. The positive control consisted of cell medium and cells. In the negative control the cells were incubated in 1 ml 70% ethanol for 5

minutes prior to the staining. After incubation the ethanol was removed from the wells and the negative control wells were washed twice with DPBS. In the last control group the well plates were covered with gelatin solution (10% w/v). A stock solution of Propidium Iodide (PI) was prepared. To do this, PI was dissolved in DPBS to obtain a 20 µg/ml concentration in the solution. Additionally, a Fluorescein Diacetate (FDA) stock solution was prepared by dissolving FDA (Thermo Fischer scientific) in acetone to obtain a 5 mg/ml concentration. Subsequently, a FDA working solution was prepared by dissolving 10 µl FDA in acetone in 2,5 ml DPBS to obtain 20 mg/ml as final concentration. 30 µl of PI in DPBS (20 mg/ml) stock solution and 100 µl of the FDA in acetone (20 mg/ml) working solution were added to each well. The samples were incubated for 10 minutes. After incubation, the staining solution was removed and each well was washed 2 times with 1 ml DPBS.

The scaffolds were imaged on glass slides while the controls were imaged in the 24-well plate.

The cells were observed using a fluorescent microscope (Carl Zeiss) after day 1, 4 and 7. FDA-stained (live) and PI-stained (dead) cells were observed on the scaffolds. Additionally, the living cells were observed on the scaffold.

2.6.3 Cell adhesion

Cell adhesion was examined in 3 groups of PCL scaffolds: untreated scaffolds, plasma treated scaffolds and gelatin coated scaffolds. The cells were visualized as described in the cell viability experiment. To ensure only attached cells were visualized, scaffolds were removed from the wells and placed on a glass slide.

2.6.4 Cell proliferation

An AlamarBlue assay was performed to check cell proliferation rate. If the non-fluorescent AlamarBlue reagent is incubated together with viable cells, it will change its colour from blue to red due to reduction. Furthermore, it becomes fluorescent. AlamarBlue (Thermo Fischer Scientific) was added to every well containing a scaffold with ratio 1:10 to the culturing medium. Negative controls consisted of cell culture medium without scaffolds. The positive controls were cells seeded in the 24-well plate in culture medium without cells. The samples were incubated for 3,5 hour in the incubator (37°C). After the incubation time, the medium with AlamarBlue was transferred to a new well plate. The absorbance was measured by a microplate reader (Tecan, Spark 10M) using a 570 nm wavelength and 600 nm wavelength as a reference wavelength. The measurements took place on day 1, 4 and 7 after cell seeding.

2.7 Statistical analysis

Statistical analysis was carried out using a one-way Anova for the mechanical testing results and a two-way Anova for the AlamarBlue cell proliferation results. If $p \leq 0,5$ the value was considered statistically significant. The normality was tested using a Kolmogorov-Smirnov test.

3 Results

3.1 MEW

Figure 3. shows scaffolds printed with varying collector plate speed (Fig. 3A-F). The fiber alignment was worse at higher speeds (Fig. 3D-F). 60 mm/s is the highest speed at which the fibers are well-aligned on top of each other (Fig. 3C). Moreover, with increasing speeds the fibers have smaller diameters, making it more difficult to detach the scaffolds from the collector plate. These detachment problems together with a smaller fiber diameter explain why the fibers look less straight in scaffolds printed at 60 mm/s or higher speeds. Furthermore 8 layered scaffolds with different pore sizes were printed. In the scaffolds with a 100 μm pore size some deviations in the fiber alignment are visible (Fig. 4A). The scaffolds with a 200 μm and 300 μm pore size showed well aligned fibers (Fig. 4B-C). Both the 16 layered scaffold, 200 μm pore size and the 24 layered scaffold, 300 μm pore size look mostly aligned, but show also some deviations in the fiber alignment (Fig. 4D-E). Finally, a rhombus design also displayed good alignment of the fibers (Fig. 4F).

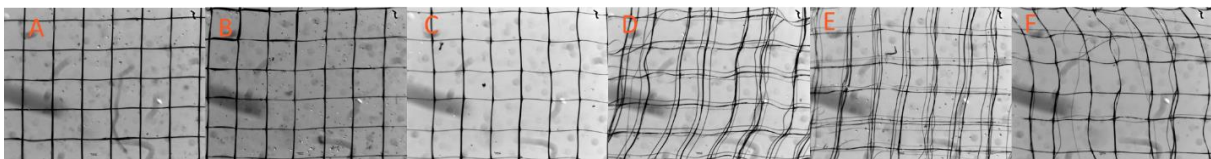


Figure 3. Scaffolds printed with varying collector speeds: (A) 20 mm/s, (B) 40 mm/s, (C) 60 mm/s, (D) 80 mm/s, (E) 100 mm/s, (F) 120mm/s.

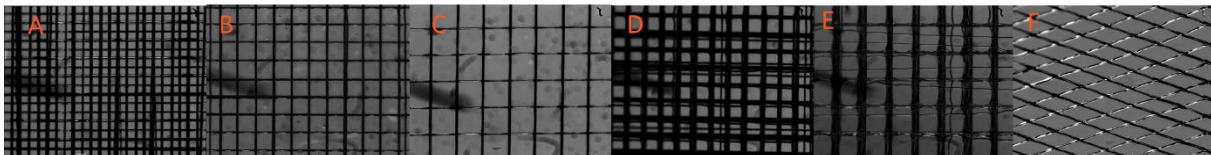


Figure 4. Scaffolds with varying pore sizes, number of layers and design. 8 layered scaffold with different pore sizes: (A) 100 μm , (B) 200 μm , (C) 300 μm . (D) 16 layers, 200 μm pore size, (E) 24 layers, 300 μm pore sizes, (F) 8 layers, 70 degree rhombus design.

After the scaffolds are fabricated using MEW it is required to gain more knowledge about their properties to examine how suitable they are for tissue engineering applications. One of the tests to check the mechanical properties of scaffolds is uniaxial tensile testing. With the use of mechanical testing the Young's modulus of the scaffolds can be obtained. The Young's modulus (E) is a variable which represents the stiffness of a material. In other words, it tells how easily a material can be stretched and deformed. Different Young's moduli were compared to examine which scaffolds will be the best option for a hard-soft tissue replacement. Two gradient scaffolds were obtained in this research: gradient 1 (Fig. 5D) and gradient 2 (Fig. 5G). Mechanical testing showed no statistical difference in Young's modulus between the different zones of the gradient scaffolds (Fig. 6A-B). However, the gradient 1 scaffold showed different results in the order of zone stretching. For one sample, both the zone 1 (Fig. 5A) and zone 3 (Fig. 5C) started to stretch first (Fig. 5E). The other two samples showed either initial stretching in only zone 1, or more in zone 2 (Fig. 5B) of the scaffold. In the gradient 1 scaffold, there was no statistical difference in Young's modulus between each zone (Fig. 5A). In the gradient 2 scaffold, zone 1 (Fig. 5H) started to stretch first in all samples (Fig. 5F). Next, zone 2 (Fig. 5I) started to stretch. Finally zone 3 (Fig. 5J) started to stretch. In the gradient 2 scaffold, there was also no statistical difference in Young's modulus between each zone (Fig. 5B). Gradient 1 has the highest average Young's modulus: $5,47 \pm 2,12$ MPa. The square 250 μm , rhombus 500 μm is the individual zone with the highest average Young's modulus: $6,25 \pm 0,79$ MPa (Fig. 6A-B).

Both scaffold designs showed in their stress-strain curve that indeed a gradient scaffold was created. The curve goes up, flattens and then goes up again (Fig. 6C-D). This shows that different zones started to stretch at different points. At the end of the graph there is some distortion visible, the stress-strain graph goes up and down. This is due to machine inconsistencies. The machine is connected to another

device which will also be lifted at a high displacement, the lifting of this device causes the inconsistencies in the graph.

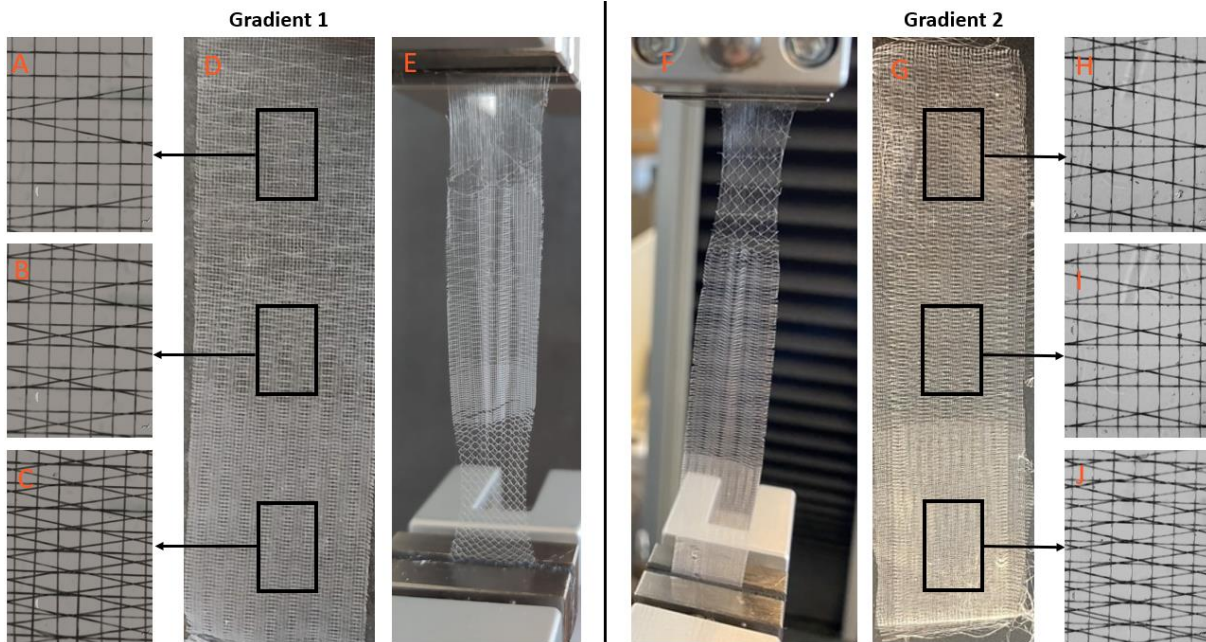


Figure 5. Two different gradient structures consisting each of 3 different zones. All rhombus structures have an angle of 159° . The different zones are visualized next to the corresponding scaffolds. (A) square 250 μm , rhombus 1250 μm , (B) square 250 μm , rhombus 500 μm , (C) square 250 μm , rhombus 250 μm , (D) full scaffold, (E) scaffold in tensile testing machine, starting to stretch at both upper and lower zone. (F) scaffold in tensile testing machine, only upper zone starts to stretch, (G) full scaffold, (H) rectangular: 250x1000 μm , rhombus 500 μm , (I) rectangular 250x500 μm , rhombus 500 μm (J) square 250x250 μm , rhombus 250 μm .

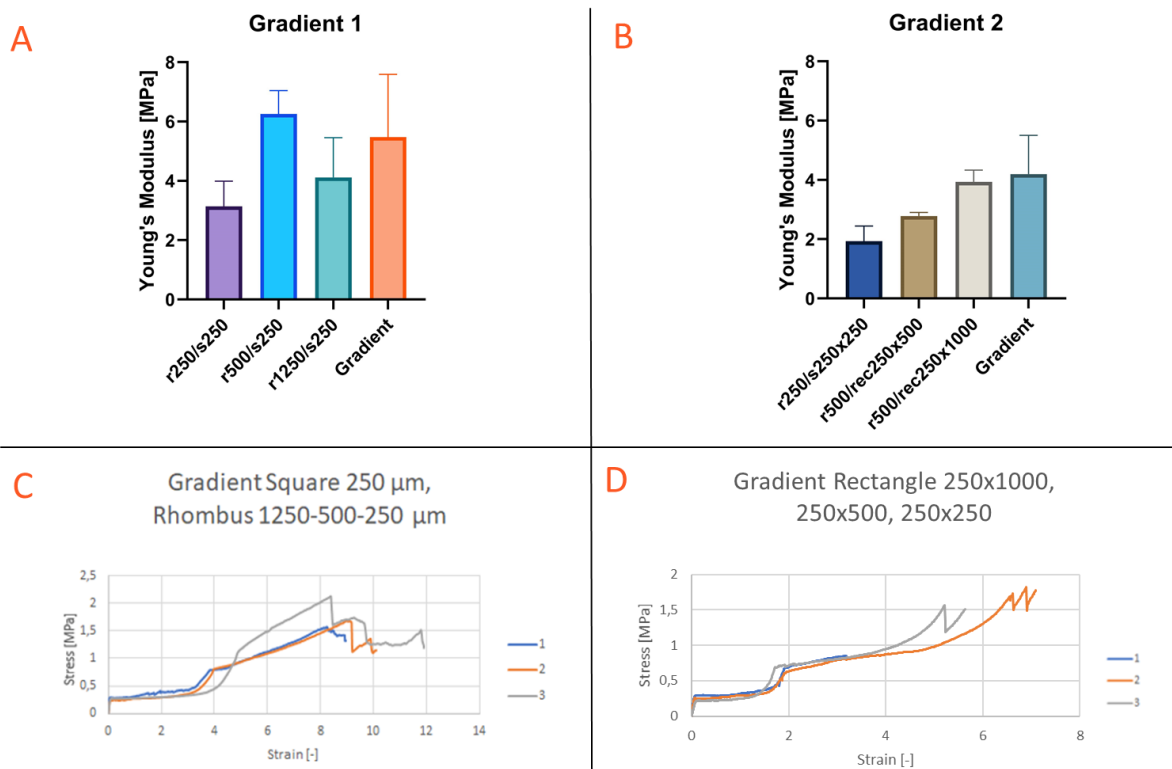


Figure 6. Mechanical properties of both gradient scaffolds: (A - B) Young's modulus for gradient scaffolds and individual zones of the gradient scaffolds. (C - D) stress - strain curve of the gradient scaffolds.

SEM pictures were obtained of the scaffold after mechanical testing. The pictures visualized what happened at the connection points of the scaffolds after tensile testing until failure. Fig. 7C shows what happens at a connection where the fibers cross each other in a 90° angle. The diameter of the fiber in tensile direction is getting smaller while the diameter of the fibers perpendicular to the tensile test direction is only changing at the connection point. The fibers in the square part of the design are still firmly attached. At connection points where fibers cross each other also at other angles than 90° (rhombus + square fibers) there is more change in the structure visible (Fig. 7D). The fibers from the rhombus design were shifted away from the nodes. Due to the displacements of fibers, the structure of the fibers got damaged. There are clear marks on the surface of the fibers, which indicate the movement of the fibers from the rhombus design during tensile testing. Furthermore, the SEM pictures showed fibers getting loose at the connection points but no broken fibers were observed.

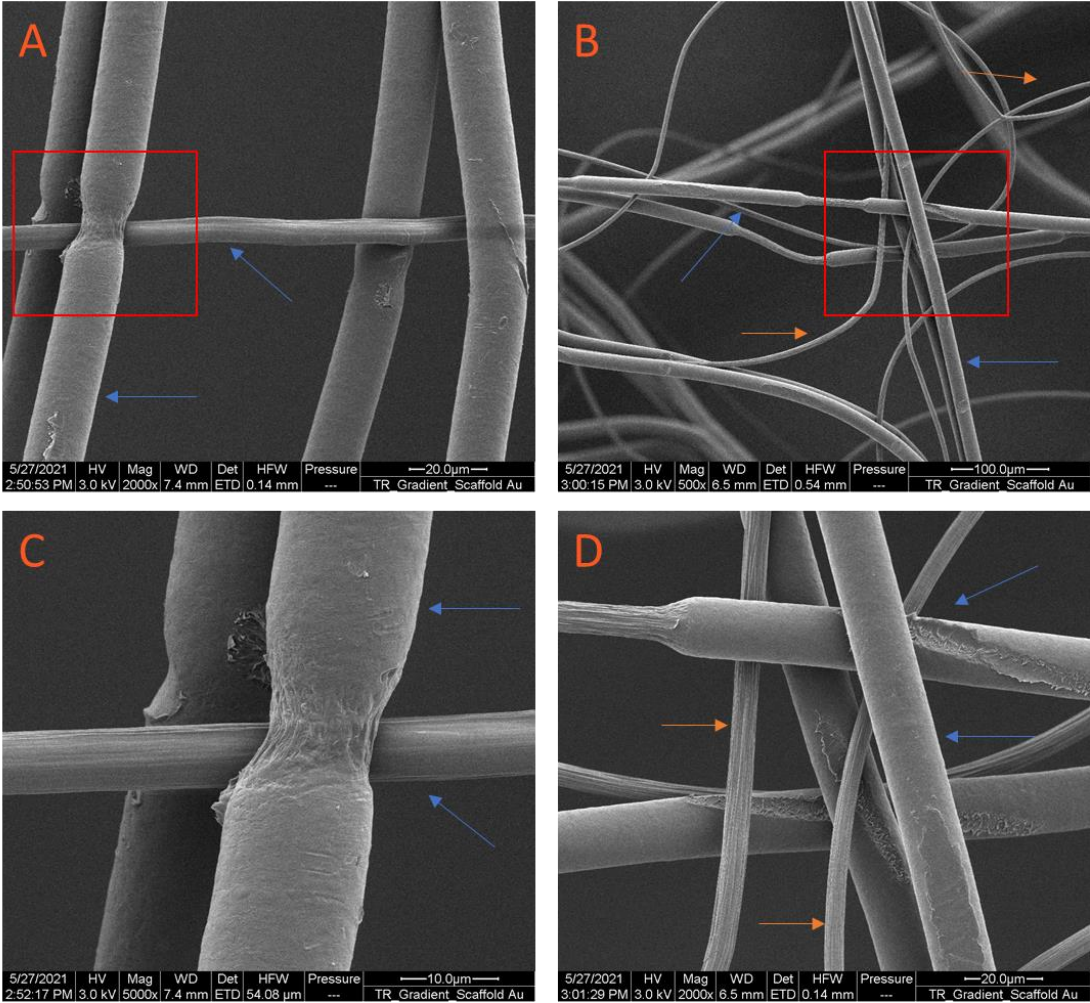


Figure 7. SEM pictures of a gradient 1 scaffold after tensile testing. Blue arrows indicate fibers from the square part of the design, orange arrows indicate the rhombus part. The red squares in (A-B) show at which place the more closer pictures are taken (C-D). (C) In square parts of the scaffolds the fibers get smaller at the nodes. (D) In square + rhombus part of the scaffold, not all fibers are connected anymore at the nodes. Furthermore, more damage to the fibers is visible.

3.2 Cell studies

In Fig. 8 the live cells on the scaffolds are visible. Already on the first day some cells are attached on the scaffold (Fig. 8, Live, Day 1). On the 7th day the amount of cells on the scaffolds has increased (Fig. 8, Live, Day 7). On both the plasma treated and the gelatin coated scaffolds it was visible that the cells started to close the pores. In these two groups the fibroblasts also started to elongate (Fig. 8, Live, Day 7, Plasma treated scaffolds and gelatin coated scaffolds). The highest number of dead cells were observed on the scaffolds coated with gelatin (Fig. 8, Dead, Gelatin coated scaffolds). However, this amount did not affect the experiment.

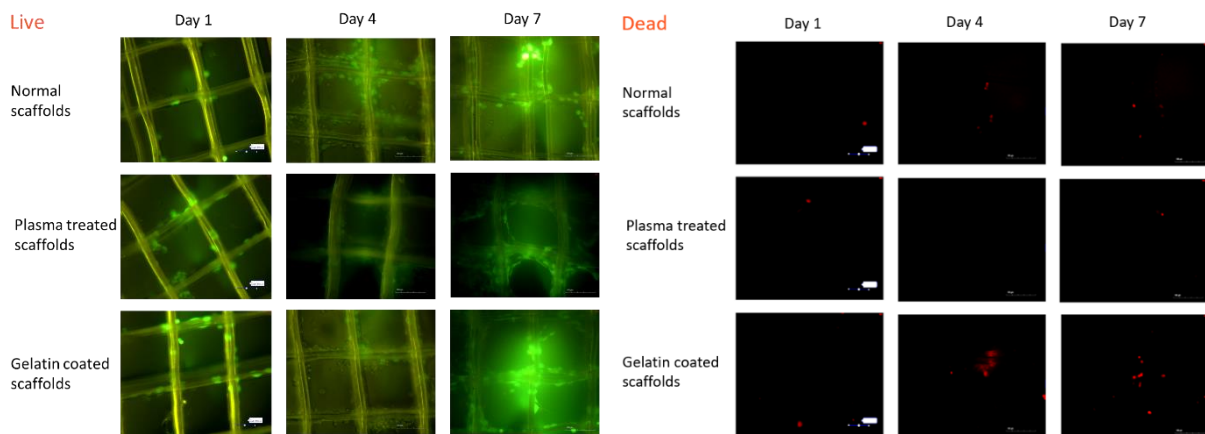


Figure 8. On the left, living cells on the scaffolds are shown in green. On the right, dead cells on the same places in the scaffolds are visible in red. Three different groups of scaffolds were tested: normal scaffolds, plasma treated scaffolds and gelatin coated scaffolds. The scaffolds together with the cells were pictured at day 1, day 4 and day 7 after cell seeding. Cells are able to attach and grow on all scaffolds.

The AlamarBlue assay showed on all control days a reagent reduction. However, during a 7 day period there was no statistical difference in reduction between days. Moreover, there is no significant difference between groups and the positive control for the given time points. On day 4 the error margins are relatively high (Fig. 9). On this day there were air bubbles visible in the wells.

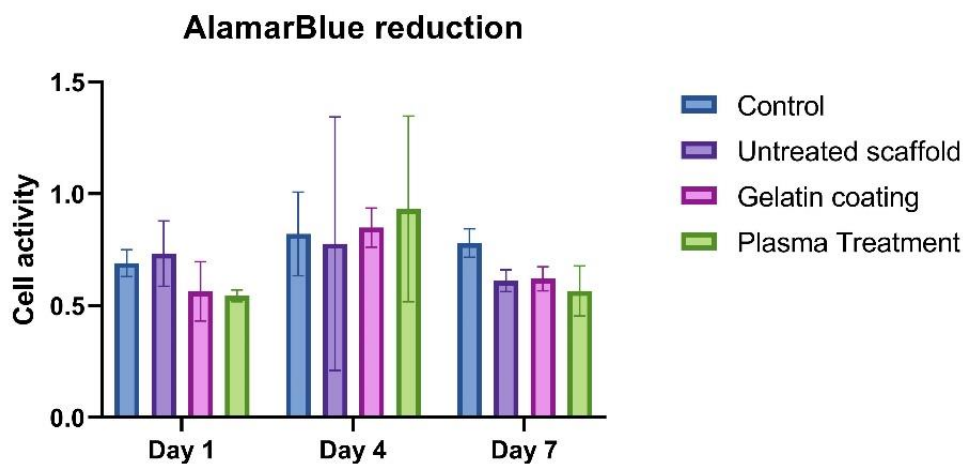


Figure 9. AlamarBlue experiment results. 4 different groups were examined: normal scaffold, gelatin coated scaffolds, plasma treated scaffolds, wells covered with gelatin. There is no statistical difference between each day and between groups on each day.

3.3 FEM

A computer model was established to obtain a Young's modulus of the simulated scaffolds. Models of scaffolds with varying pore sizes were created. The model shows in a stress plot where the stress is located in the scaffolds (Fig. 10A). In this plot, the colored parts of the geometry show the scaffolds after stretching. The colors indicate how much stress is located on each point in the scaffold. The black lines show the initial dimensions of the scaffold before simulating tensile tests. It is shown that most stress is located on the vertical fibers in tensile testing direction. Meanwhile, the stress on the horizontal fibers is practically zero. The most stress is accumulated at the nodes. Furthermore, a table of stress and strain values of the model is obtained (Fig. 10B). The Young's modulus obtained from computer simulations is in agreement with the Young's modulus from the tensile test experiments for given scaffolds. The model could predict the Young's modulus really closely. There was no statistical difference between the experimental data and COMSOL predictions (Fig. 10C). All values for E of the experimental data and from the model can be found in Table 2.

Table 2. Young's modulus 8 layered scaffold (16 μm fiber diameter) for experimental data and the model predictions.

Pore sizes of the scaffolds	E from Experimental data [MPa]	E from COMSOL [MPa]
200 μm	8,76 \pm 1,05	7,74
300 μm	5,73 \pm 0,42	5,17
500 μm	3,37 \pm 0,44	3,06

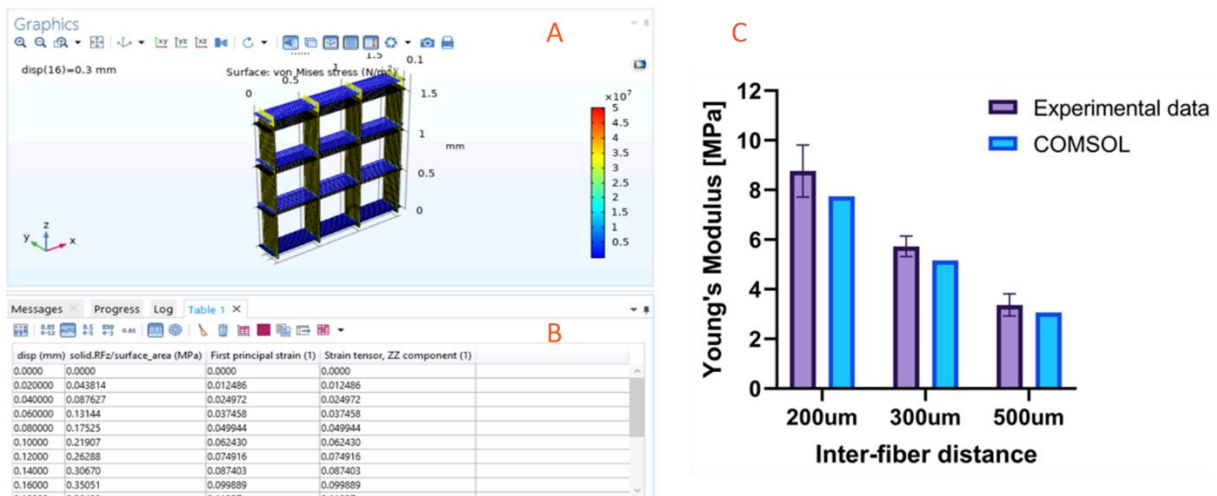


Figure 10. From scaffold to model. In the model a stress plot in the scaffold was obtained (A). In addition, a table with all stress/strain values for each displacement step (B). The experimental data from scaffolds with different pore sizes is compared with data from the model (C). There was no statistical difference between the Young's modulus obtained from the model and experimental data.

3.4 Application

An application was created for the scaffold model established in this research. With the application, it is possible to create a model for scaffolds with different properties. A new model can be created merely by changing parameters related to the desired change in scaffold geometry. The geometry will update automatically and the results can be obtained. An outlook of the application together with all parameters which can be changed can be found in Fig. 11A. The application will also display a stress plot to show where the stress is located in the scaffold. Furthermore, a table of the stress strain values will be obtained after calculating. In addition to these results a detailed report about the model and the results can be obtained. An example of this report for an 8 layered scaffold with a 200 μm pore size can be found in *Appendix A*. Before computing the studies, the geometry can be plotted to

investigate the effect of the changed parameters on the geometry (Fig. 11B). To examine if a change in parameters indeed led to a similar change in geometry, parameters have been changed and the change in geometry has been observed. The following changes were applied to the model. The number of layers was increased to 16 (Fig. 11C), the radius of the fibers increased from 0,008 mm to 0,016 mm (Fig. 11D), the connected part of the fibers was increased from 2 μm to 6 μm (Fig. 11E) and the pore size was increased from 0,2 mm to 0,5 mm (Fig. 11F). It is shown that the geometry is updated correctly corresponding to the new parameters.

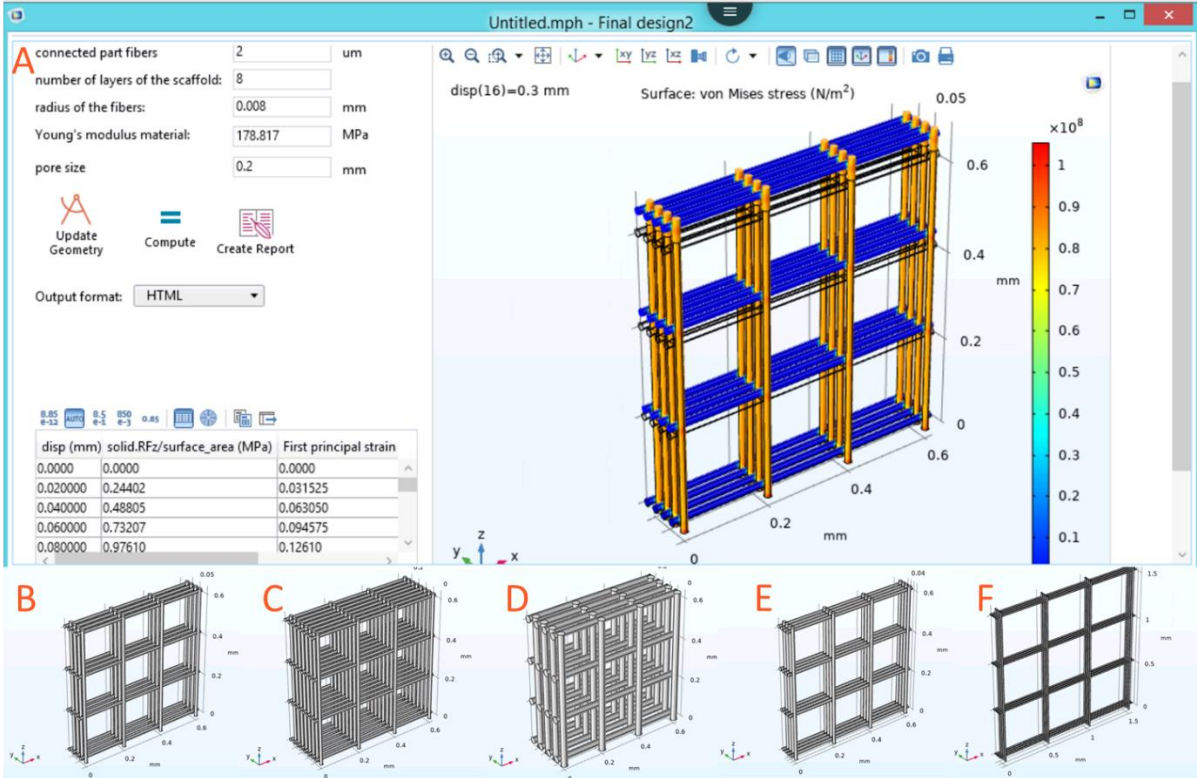


Figure 11. Application of the model shows (A) the application itself after computing, (B) the geometry used for this computation. Furthermore, the following scaffold properties can be changed in the model: (C) number of layers (16), (D) radius of the fibers (0.016 mm), (E) Connected part of the fibers (6 μm), (F) pore size (0.5 mm)

4 Discussion and conclusion

In this research it is shown that it is possible to create gradient scaffolds using MEW. Furthermore, the attachment of cells on PCL scaffolds is shown. Gelatin coating and plasma treatment seem to improve this attachment. Moreover, a computer model of PCL scaffolds is established. With this model it is possible to make precise predictions about the Young's modulus of scaffolds. In addition to the model an application is created, which enhances the process of simulating scaffolds with varying topological properties. The application allows to change the following properties of the scaffold model: pore size, connected part of the fibers, radius of the fibers, number of layers and Young's modulus of the material.

The results from the printing of different designs showed that the printing speed, the pore size and the number of layers have an impact on the printing accuracy. The lower printing accuracy for scaffolds with a higher amount of layers can be explained by periodic defects caused by charge accumulation. As the number of layers of a scaffold increase, the residual charges will have a higher effect on the printing accuracy. It will cause repelling of the printed fibers, which will lead to a less aligned deposition of fibers [23]. Another cause for the inaccuracies might be a lag of the printing jet. A solution for this problem might be to update the printing pathway for every printed layer. Liashenko et al. showed that this so-called 'microscale layer shifting' can be used to obtain a higher printing accuracy. Furthermore, it allows the printing of nonlinear and geometrical advanced structures [24]. In addition to printing square scaffolds with varying properties, other shapes than squares were printed to investigate the different possibilities of MEW. The alignment of these shapes was examined. It is shown that besides squared scaffolds, MEW is also able to create a nicely aligned rhombus structure and a combination of the rhombus and square designs.

The gradient 2 scaffold (Fig. 5G) clearly showed that each zone started to stretch at different points. This indicates that this scaffold has gradient properties. This can be useful for the creation of scaffolds for hard-soft tissue interfaces. The zone of the scaffold with the highest density in horizontal/rhombus fibers started to stretch the latest. These results are in line with previous research, which has shown that crosslinking increases the mechanical properties of tendons [25]. The other gradient 1 (Fig. 5D) scaffold showed a more random distribution of which zone started to stretch first. Additionally in this scaffold there were smaller differences between zones. In gradient 1 there was only a difference between zones in the rhombus shapes, while in gradient 2 there was also a difference in rectangular shapes. Gradient 1 showed that different zones started to stretch first. Meanwhile, in gradient 2 zone 1 always started to stretch first. Therefore, these results from mechanical testing imply that changing the interfiber distance in the rectangular shapes has a larger effect on the mechanical properties of the scaffold than changing the interfiber distance in the rhombus shapes. In the gradient scaffolds in this research, there was still a high amount of cross linking in the zone representing the tendon site. A reason for this was that it enables better detachment of the scaffolds from the collector plate without destroying the scaffolds. Raspanti et al. observed in their research only a few interfibrillar bridges in tendons. The fibrils are rather bound tightly together by proteoglycans [26]. For future gradient scaffolds it can be interesting to also print scaffolds where the tendon site has a lower amount of cross linking or no cross linking of the fibers. However, it will be a challenge to find a method on how to keep the fibers packed closely together. The disadvantage of low amount or no crosslinking is that due to static forces, it will be hard to detach the fibers and keep them together.

While gradient scaffolds show to have potential in distributing the load in different zones, their Young's modulus still remains lower than the original hard-soft tissue. Thus, it might be useful to look into how these scaffolds can be improved in the future. Since the fibers were getting loose first at the nodes, this is a place which can be improved. Possible with a coating the fibers can be connected better. In general, a coating can lead to better mechanical properties. Xie et al. proved this point in their research. They

increased the Young's modulus of PCL fiber samples from 86 MPa to 768 MPa (tensile tests) by applying a coating. A polydopamine coating was used to induce biomineralization of the PCL fibers, leading to higher ultimate tensile strength, stiffness and toughness [27]. In this study a gradient structure was developed, where the gradient depends on the design rather than the composition of the scaffold. In addition to a gradient in the design, a gradient in the composition might also be really useful to create an even better gradient. Li et al. showed in their study that it is possible to create a gradient coating of calcium phosphate. This gradient yielded also a gradient in the stiffness of the material [28].

It might also be that if a greater part of the fibers is interconnected, the fibers are connected more firmly. Because of this, the connection points can possibly withstand more stress before the fibers are disjoining. These are matters where the model can be of good use, since in the model the amount of interconnection can be changed. Thus, it can be predicted if the amount of interconnection can make a significant difference in scaffold properties. In general the model shows high potential for predicting values of scaffolds.

Furthermore, it was important to consider what mesh is used for the model because COMSOL performs a finite element analysis (FEM) to obtain the results. With FEM a structure is divided into many small structures and for each small structure the equations of the applied physics are solved. A finer mesh means a more accurate calculation, but also a longer calculation time. In contrast, a coarse mesh will compute the results faster but with lower accuracy. In this model a fine mesh was used, it might be that a finer mesh gives even more precise prediction.

One explanation for the difference between model and experimental data is that the model will always assume that everything is perfect. In the real world, printing will not always be perfect and some inaccuracies can occur. Hence, there will still be a small difference between model and experimental data. Nonetheless, the application will make it considerably easier to predict values in the future for a large amount of different scaffolds. Thus modelling can certainly assist in designing scaffolds.

The live/dead staining pictures showed that the cells are attached on the scaffold. According to the images (Fig. 8, Live), it seemed that the cells were growing and proliferating in time. The results of the cell studies implied that untreated, plasma treated and gelatin coated PCL scaffolds are not toxic for cells. Furthermore, this study suggested the scaffolds are not toxic and can support fibroblast proliferation and adhesion. To examine the *in vitro* cytotoxicity 3T3 fibroblasts were used in this study. However, for a final application, a scaffold which can replace the tendon to bone connection site, it might be useful to use other cell types in future studies. Adipose-derived stem cells (ADSCs) have great potential to create a gradient in the cell types. Due to their pluripotent nature, they can differentiate to osteoblasts (bone-forming) as well as fibroblasts (tendon-forming). Furthermore, ADSCs have a high proliferation rate and are also able to deposit extracellular matrix [29, 30]. On top of this, treatment with growth differentiation factor 5 (GDF-5) can increase the expression of collagen type I encoding genes by fourfold, within a week [31].

The cell proliferation experiments however, showed no statistical difference between the control days. This indicates that the cells are not growing in time. Day 4 of the AlamarBlue assay showed higher error bars in comparison with the other days (Fig. 9.) On this day, there were air bubbles in the medium. These bubbles might have caused the difference in results due to light scattering. Furthermore, an excess of cells was used, to make sure cells would adhere to the scaffolds. This might give an explanation about why the AlamarBlue assay did not show growth of the cells in time. In this assay all the cells in the wells were measured, not only the one on the scaffolds. For future studies it is recommended to move the scaffolds to another well before starting an AlamarBlue assay. This should ensure that only cells on the scaffolds are measured.

For future research it would be of great use to validate the model for different scaffold properties. In this research it is shown that the model can predict values closely for scaffolds with varying pore sizes. However, since the application also allows change of other parameters rather than pore size, it would be beneficial to know if these predictions are similarly close to the experimental data. Furthermore, it would be valuable to expand the application by adding more functionality. A proposed additional

feature for the application would be to automatically calculate the Young's modulus from the data in the table. If this is possible, it can accelerate the process of comparing scaffolds with varying topological properties. This would be of great use in the search for scaffolds with optimal mechanical properties.

6 References

1. Seidi, A., et al., *Gradient biomaterials for soft-to-hard interface tissue engineering*. Acta biomaterialia, 2011. **7**(4): p. 1441-1451.
2. Pajala, A., et al., *Rerupture and deep infection following treatment of total Achilles tendon rupture*. JBJS, 2002. **84**(11): p. 2016-2021.
3. KANNUS, P., *Tendon injuries and other tendon disorders in sports and exercise*. Scandinavian journal of medicine & science in sports, 1997. **7**(2).
4. Longo, U.G., et al., *Acute achilles tendon rupture in athletes*. Foot and ankle clinics, 2013. **18**(2): p. 319-338.
5. Houshian, S., T. Tscherning, and P. Riegels-Nielsen, *The epidemiology of Achilles tendon rupture in a Danish county*. Injury, 1998. **29**(9): p. 651-654.
6. Inglis, A.E. and T.P. Sculco, *Surgical repair of ruptures of the tendo Achillis*. Clinical orthopaedics and related research, 1981(156): p. 160-169.
7. Linderman, S.W., et al., *Enhanced tendon-to-bone repair through adhesive films*. Acta biomaterialia, 2018. **70**: p. 165-176.
8. Lanza, R., et al., *Principles of tissue engineering*. 2020: Academic press.
9. Griffith, L.G. and G. Naughton, *Tissue engineering--current challenges and expanding opportunities*. science, 2002. **295**(5557): p. 1009-1014.
10. Birch, H.L., *Tendon matrix composition and turnover in relation to functional requirements*. International journal of experimental pathology, 2007. **88**(4): p. 241-248.
11. Thorpe, C.T., et al., *Anatomical heterogeneity of tendon: Fascicular and interfascicular tendon compartments have distinct proteomic composition*. Scientific reports, 2016. **6**(1): p. 1-12.
12. Benjamin, M., E.J. Evans, and L. Copp, *The histology of tendon attachments to bone in man*. Journal of anatomy, 1986. **149**: p. 89.
13. Yang, P.J. and J.S. Temenoff, *Engineering orthopedic tissue interfaces*. Tissue Engineering Part B: Reviews, 2009. **15**(2): p. 127-141.
14. Lu, H.H. and J. Jiang, *Interface tissue Engineering and the formulation of multiple-tissue systems*. Tissue Engineering I, 2005: p. 91-111.
15. Zhao, H., et al., *Ultrasonic evaluations of Achilles tendon mechanical properties poststroke*. Journal of applied physiology, 2009. **106**(3): p. 843-849.
16. Ding, M., et al., *Mechanical properties of the normal human tibial cartilage-bone complex in relation to age*. Clinical Biomechanics, 1998. **13**(4-5): p. 351-358.
17. Tellado, S.F., E.R. Balmayor, and M. Van Griensven, *Strategies to engineer tendon/ligament-to-bone interface: Biomaterials, cells and growth factors*. Advanced drug delivery reviews, 2015. **94**: p. 126-140.
18. Williams, J., *Achilles tendon lesions in sport*. Sports Medicine, 1986. **3**(2): p. 114-135.
19. Hochleitner, G., et al., *Melt electrowriting of thermoplastic elastomers*. Macromolecular rapid communications, 2018. **39**(10): p. 1800055.
20. Eshraghi, S. and S. Das, *Mechanical and microstructural properties of polycaprolactone scaffolds with one-dimensional, two-dimensional, and three-dimensional orthogonally oriented porous architectures produced by selective laser sintering*. Acta biomaterialia, 2010. **6**(7): p. 2467-2476.
21. Rosa, D., C. Guedes, and M. Bardi, *Evaluation of thermal, mechanical and morphological properties of PCL/CA and PCL/CA/PE-g-GMA blends*. Polymer Testing, 2007. **26**(2): p. 209-215.
22. Jones, K.H. and J.A. Senft, *An improved method to determine cell viability by simultaneous staining with fluorescein diacetate-propidium iodide*. Journal of Histochemistry & Cytochemistry, 1985. **33**(1): p. 77-79.
23. Wunner, F.M., et al., *Melt electrospinning writing of highly ordered large volume scaffold architectures*. Advanced Materials, 2018. **30**(20): p. 1706570.

24. Liashenko, I., A. Hrynevich, and P.D. Dalton, *Designing outside the box: Unlocking the geometric freedom of melt electrowriting using microscale layer shifting*. *Advanced Materials*, 2020. **32**(28): p. 2001874.
25. Maffulli, N., H. Moller, and C.H. Evans, *Tendon healing: can it be optimised?* *British journal of sports medicine*, 2002. **36**(5): p. 315-316.
26. Raspanti, M., T. Congiu, and S. Guizzardi, *Structural aspects of the extracellular matrix of the tendon: an atomic force and scanning electron microscopy study*. *Archives of histology and cytology*, 2002. **65**(1): p. 37-43.
27. Xie, J., et al., *Controlled biomineralization of electrospun poly (ϵ -caprolactone) fibers to enhance their mechanical properties*. *Acta biomaterialia*, 2013. **9**(3): p. 5698-5707.
28. Li, X., et al., *Nanofiber scaffolds with gradations in mineral content for mimicking the tendon-to-bone insertion site*. *Nano letters*, 2009. **9**(7): p. 2763-2768.
29. Bodle, J.C., A.D. Hanson, and E.G. Lobo, *Adipose-derived stem cells in functional bone tissue engineering: lessons from bone mechanobiology*. *Tissue Engineering Part B: Reviews*, 2011. **17**(3): p. 195-211.
30. Tapp, H., et al., *Adipose-derived stem cells: characterization and current application in orthopaedic tissue repair*. *Experimental biology and medicine*, 2009. **234**(1): p. 1-9.
31. James, R., et al., *Tendon tissue engineering: adipose-derived stem cell and GDF-5 mediated regeneration using electrospun matrix systems*. *Biomedical materials*, 2011. **6**(2): p. 025011.

Appendix A Report COMSOL model

8 layers, 200 μm pore size

Report date

Jun 25, 2021 3:31:08 PM

Contents

1. Global Definitions	27
1.1. Parameters	27
2. Component 1	28
2.1. Definitions	28
2.2. Geometry 1	28
2.3. Materials	29
2.4. Solid Mechanics	29
2.5. Mesh 1	30
3. Study 1	31
3.1. Stationary	31
4. Results	33
4.1. Datasets	33
4.2. Derived Values	33
4.3. Tables	34
4.4. Plot Groups	35

1 Global Definitions

Date	Jun 21, 2021 5:08:43 PM
------	-------------------------

Global settings

Name	Untitled.mph
Version	COMSOL Multiphysics 5.5 (Build: 292)

Used products

COMSOL Multiphysics

1.1 PARAMETERS

Parameters 1

Name	Expression	Value	Description
YM	178[MPa]	1.78E8 Pa	
width	h1	6.4E-4 m	
thickness	y_num*y_dis + 2*con	1.16E-4 m	
surface_area	width*thickness	7.424E-8 m ²	
con	2[um]	2E-6 m	Amount of connection between fibers
dens1	1145	1145	Density
disp	0.3[mm]	3E-4 m	Displacement
y_dis	(2*rad1) - con	1.4E-5 m	distance between layers
x_dis	0.2[mm]	2E-4 m	distance between the (centers of) fibers
h1	x_num*x_dis - ((4/5)*x_dis)	6.4E-4 m	length of the fibers
x_num	4	4	number of fibers next to each other
y_num	8	8	number of layers of the scaffold
pois1	0.3	0.3	Poisson's ration
rad1	0.008[mm]	8E-6 m	radius of the fibers
E1	178.817[MPa]	1.7882E8 Pa	Young's modulus material

2 Component 1

2.1 DEFINITIONS

2.1.1 Coordinate Systems

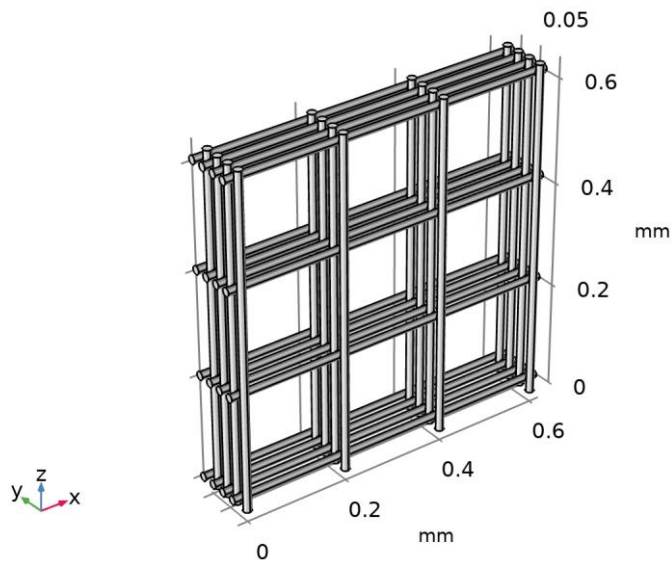
Boundary System 1

Coordinate system type	Boundary system
Tag	sys1

Coordinate names

First	Second	Third
t1	t2	n

2.2 GEOMETRY 1



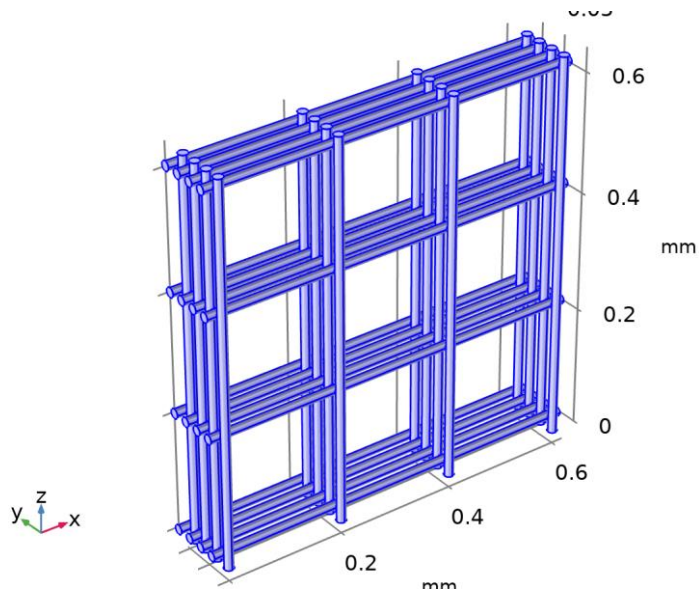
Geometry 1

Units

Length unit	mm
Angular unit	deg

2.3 MATERIALS

2.3.1 PCL

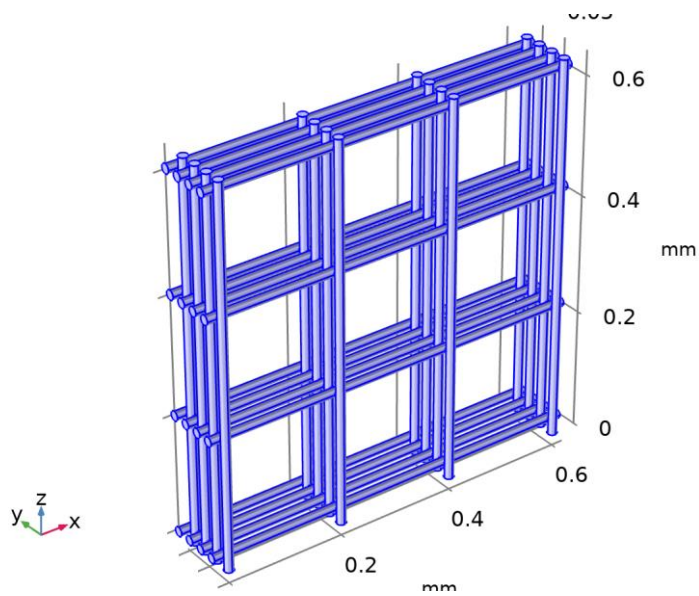


PCL

Selection

Geometric entity level	Domain
Selection	Geometry geom1: Dimension 3: All domains

2.4 SOLID MECHANICS



Solid Mechanics

Equations

$$0 = \nabla \cdot \mathbf{S} + \mathbf{F}_v$$

Features

Linear Elastic Material 1
Free 1
Initial Values 1
Fixed Constraint 1
Prescribed Displacement 1

2.4.1 Linear Elastic Material 1

Equations

$$\begin{aligned} \underline{\underline{0}} &= \nabla \cdot \underline{\underline{S}} + \underline{\underline{F}}_V \\ \underline{\underline{S}} &= \underline{\underline{S}}_{ad} + \underline{\underline{C}} : \underline{\underline{\epsilon}}_{el}, \quad \underline{\underline{\epsilon}}_{el} = \underline{\underline{\epsilon}} - \underline{\underline{\epsilon}}_{inel} \\ \underline{\underline{\epsilon}}_{inel} &= \underline{\underline{\epsilon}}_0 + \underline{\underline{\epsilon}}_{ext} + \underline{\underline{\epsilon}}_{th} + \underline{\underline{\epsilon}}_{hs} + \underline{\underline{\epsilon}}_{pl} + \underline{\underline{\epsilon}}_{cr} + \underline{\underline{\epsilon}}_{vp} \\ \underline{\underline{S}}_{ad} &= \underline{\underline{S}}_0 + \underline{\underline{S}}_{ext} + \underline{\underline{S}}_q \\ \underline{\underline{\epsilon}} &= \frac{1}{2} \left[(\nabla \underline{\underline{u}})^T + \nabla \underline{\underline{u}} \right] \\ \underline{\underline{C}} &= \underline{\underline{C}}(E, \nu) \end{aligned}$$

2.4.2 Fixed Constraint 1

Equations

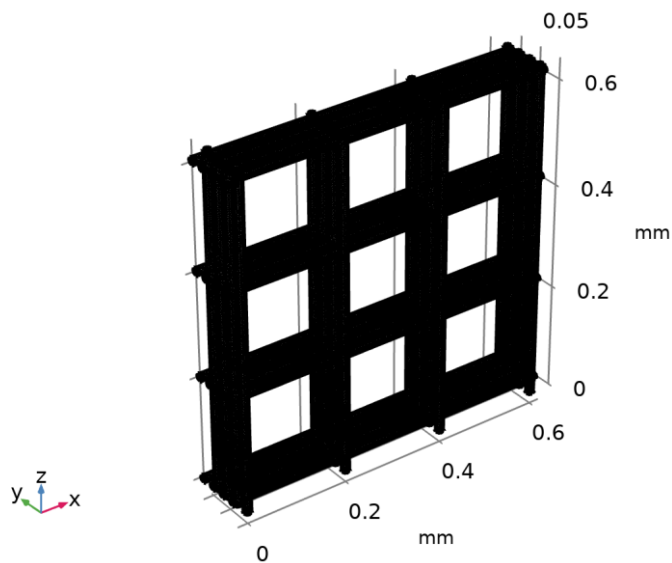
$$\underline{\underline{u}} = \underline{\underline{0}}$$

2.4.3 Prescribed Displacement 1

Equations

$$u_z = u_{0z}$$

2.5 MESH 1



Mesh 1

3 Study 1

Computation information

Computation time	
CPU	Intel64 Family 6 Model 79 Stepping 0, 6 cores
Operating system	Windows Server 2012 R2

3.1 STATIONARY

Study settings

Description	Value
Include geometric nonlinearity	Off

Study extensions

Description	Value
Auxiliary sweep	On
Sweep type	Specified combinations
Run continuation for	No parameter

Parameters

Parameter name	Parameter value list	Parameter unit
disp (Displacement)	range(0,0.02,0.3)	mm

Physics and variables selection

Physics interface	Discretization
Solid Mechanics (solid)	physics

Mesh selection

Geometry	Mesh
Geometry 1 (geom1)	mesh1

3.1.1 Study extensions

Study extensions

Description	Value
Auxiliary sweep	On
Sweep type	Specified combinations
Run continuation for	No parameter

Parameters

Parameter name	Parameter value list	Parameter unit
disp (Displacement)	range(0,0.02,0.3)	mm

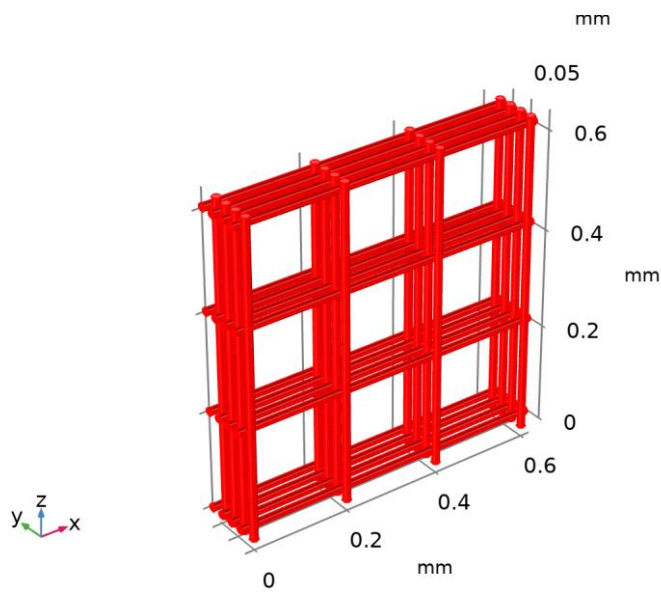
4 Results

4.1 DATASETS

4.1.1 Study 1/Solution 1

Solution

Description	Value
Solution	Solution 1
Component	Save Point Geometry 1



Dataset: Study 1/Solution 1

4.2 DERIVED VALUES

4.2.1 Surface Integration 1

Output

Evaluated in	Table 1
--------------	-------------------------

Data

Description	Value
Dataset	Study 1/Solution 1

Expressions

Expression	Unit	Description
solid.RFz/surface_area	MPa	

Expressions

Name	Value	Unit	Description
solid.refpntx	m		Reference point for moment computation, x coordinate
solid.refpnty	m		Reference point for moment computation, y coordinate
solid.refpntz	m		Reference point for moment computation, z coordinate

Integration settings

Description	Value
Integration order	4

4.2.2 Surface Average 1

Output

Evaluated in	Table 1
--------------	-------------------------

Data

Description	Value
Dataset	Study 1/Solution 1

Expressions

Expression	Unit	Description
solid.ep1	1	First principal strain
solid.eZZ	1	Strain tensor, ZZ component

Expressions

Name	Value	Unit	Description
solid.refpntx	m		Reference point for moment computation, x coordinate
solid.refpnty	m		Reference point for moment computation, y coordinate
solid.refpntz	m		Reference point for moment computation, z coordinate

Integration settings

Description	Value
Integration order	4

4.3 TABLES

4.3.1 Table 1

Surface Integration 1

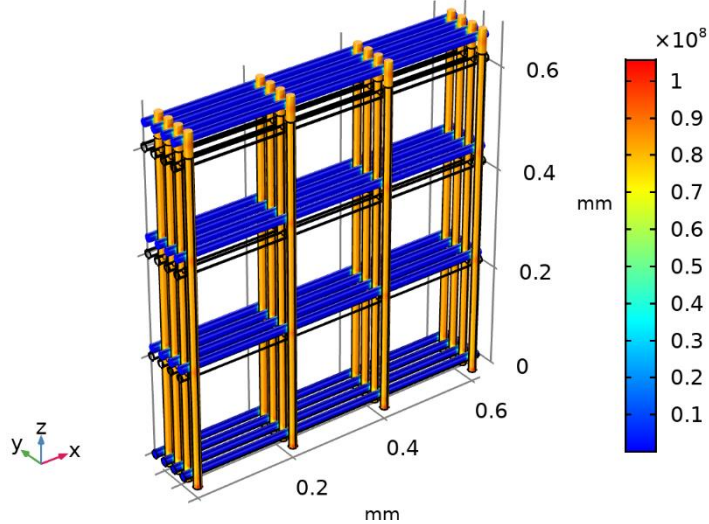
disp (mm)	solid.RFz/surface_area (MPa)	First principal strain (1)	Strain tensor, ZZ component (1)
0.0000	0.0000	0.0000	0.0000
0.020000	0.24402	0.031525	0.031525

disp (mm)	solid.RFz/surface_area (MPa)	First principal strain (1)	Strain tensor, ZZ component (1)
0.040000	0.48805	0.063050	0.063050
0.060000	0.73207	0.094575	0.094575
0.080000	0.97610	0.12610	0.12610
0.100000	1.2201	0.15762	0.15762
0.120000	1.4641	0.18915	0.18915
0.140000	1.7082	0.22067	0.22067
0.160000	1.9522	0.25220	0.25220
0.180000	2.1962	0.28372	0.28372
0.200000	2.4402	0.31525	0.31525
0.220000	2.6843	0.34677	0.34677
0.240000	2.9283	0.37830	0.37830
0.260000	3.1723	0.40982	0.40982
0.280000	3.4163	0.44135	0.44135
0.300000	3.6604	0.47287	0.47287

4.4 PLOT GROUPS

4.4.1 Stress (solid)

disp(16)=0.3 mm Surface: von Mises stress (N/m²)



Surface: von Mises stress (N/m²)